JACS
JOURNAL OF THE AMERICAN CHEMICAL SOCIETY

Article

pubs.acs.org/JACS

Porous Molecular Crystals by Macrocyclic Coordination Supramolecules

Irene Bassanetti,[†] Angiolina Comotti,*[,‡] Piero Sozzani,[‡] Silvia Bracco,[‡] Gianluca Calestani,[†] Francesco Mezzadri,[†] and Luciano Marchiò*[,†]

[†]Dipartimento di Chimica, Università degli Studi di Parma, viale delle Scienze 17/a, 43124 Parma, Italy

[‡]Department of Materials Science, University of Milano Bicocca, via Roberto Cozzi 55, 20125 Milano, Italy

Supporting Information

ABSTRACT: In this study, we show how the combination of metal ions, counter-anions and opportunely functionalized and preorganized ligands gives rise to two distinct supramolecular isomers, coordination polymeric chains and hexameric macrocycles. The hexamers then aggregate to form a cubic structure exhibiting permanent microporosity. The supramolecular assemblies are formed with Ag^+, thioether functionalized bis(pirazolyl)methane ligands and $CF_3SO_3^-/PF_6^-$ as the counter-anions. Five different ligands were prepared by modifying the peripheral thioether moiety with naphthyl, methoxy, *m*-Me, *p*-Me and F groups (L^{SNf}, L^{SPhOMe}, $L^{SPhm\text{-}Me}$, $L^{SPhp\text{-}Me}$, and L^{SPhF}). Helicoidal coordination polymeric chains are formed with $CF_3SO_3^-$ (general formula $[Ag(L)]_n(CF_3SO_3)_n$), whereas macrocyclic hexamers are formed with PF_6^- (general formula $[Ag(L)]_6(PF_6)_6$). The macrocycles self-assemble into ordered capsules with the shape of a tetrahedron, and the overall framework is sustained by $Ag^+\cdots(PF_6^-)\cdots Ag^+$ contacts. The capsules generate a highly symmetric structural arrangement, which is characterized by permanent microporosity arising from two distinct types of microporous chambers in the structure. The gas absorption isotherms show that the materials can selectively adsorb CO_2 and N_2O over CH_4 and N_2. The modulation of the microporosity of the materials is achieved by the different thioether functionalization of the ligands L^{SNf}, L^{SPhOMe}, $L^{SPhm\text{-}Me}$, and L^{SPhF}. The diffusion and localization of the gas molecules within the cavities were investigated by 2D $^1H-^{13}C$ solid state NMR on samples loaded with enriched $^{13}CO_2$, showing that both types of cavities are accessible to guest molecules from the gas phase.

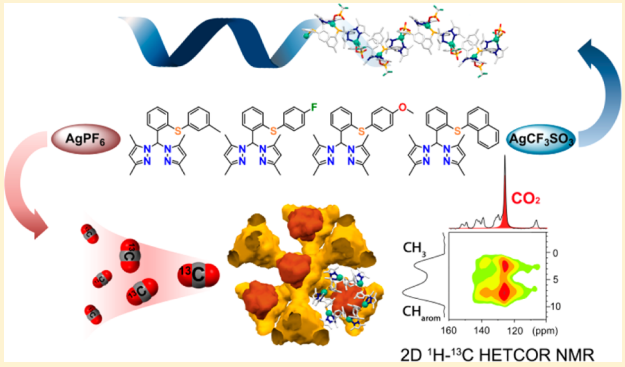

INTRODUCTION

The exploitation of robust coordination bonds is an intriguing alternative to the use of covalent bonds for the formation of discrete chemical entities (*supramolecules*)[1] and the construction of 1D, 2D and 3D coordination complexes with the shape of chains, rings, spheres, Platonic or Archimedean solids.[2] At a higher hierarchical level, coordination supramolecules can aggregate into solids by ionic or softer interactions, which govern their self-assembly into sophisticated architectures. These materials composed of supramolecules provide a versatile platform for the attainment of rich structural diversification, including the possibility of developing permanent porosity. The property of porosity and the accessibility to guest species relate to several diverse fields, such as catalysis,[3] gas capture[4] and separation,[2m] molecular recognition,[2m,n] luminescence,[5] magnetism,[6] and drug delivery.[7]

The strategy used to fabricate the coordination supramolecules and, particularly, the cyclic coordination oligomers is based on the proper choice of the ligand, the metal nodes, and the anionic counterions.[8] The design of the multitopic organic ligands, which predictably bind the metal centers, plays a central role in the development of the coordination architectures. The ligands may be rigid or flexible according to their ability to retain their shape and conformations against local stresses in the final arrangement.[9] The shape-persistent characteristic of the organic ligand may favor the cyclic macroconformation, although the key feature to induce a curvature in the metal−organic repeat-unit enchainments is the design of an appropriate nonaxially symmetric spatial distribution of the chelating functional groups in the ligand. This sophisticated molecular engineering leads to the construction of ring-shaped supramolecules of remarkable robustness.[10]

A crucial and often neglected role is played by the anion, which must be accommodated to counterbalance the positive charge of the metal, especially when neutral ligands are employed. In most cases, the counter-anions are characterized by a high symmetry (for example, NO_3^-, SO_4^{2-}, X^-, ClO_4^-, BF_4^-, and PF_6^-) and by the presence of multiple potential binding sites, thus offering the possibility to act as a linker between two metal centers. The donor atoms in the anions and

Received: July 24, 2014
Published: September 24, 2014

dx.doi.org/10.1021/ja507555j | J. Am. Chem. Soc. 2014, 136, 14883−14895

the overall size of the anion dictate the strengths of the metal-anion interactions, which may be weak and prone to dissociation in polar solvents. However, in the solid state, even large and weakly coordinating anions interposed between two metal centers can sustain the formation of stable crystal structures. The anions can profoundly modulate the arrangement of the supramolecules regarding the packing modes,[11] the topology,[12] or stabilization of complex supramolecular architectures at the highest hierarchical level.[13] Finally, the coordination numbers and the geometry imposed by the metal node significantly influence the ligand orientation and the robustness of the architecture. Metal ions, such as Pd(II), Pt(II), Co(III), Cr(III), and Fe(II), dictate the geometry of the surrounding donor atoms (e.g. square planar or octahedral). In contrast, Ag(I) exhibits diversified coordination geometries, such as linear, trigonal-planar, T-shaped, and tetrahedral, which lead to a variety of architectures with tailored structures and functions.[14] This variety implies that Ag(I) can be considered as a "flexible" node and can adapt to a specific ligand preorganization and an attractive metal node for the construction of coordination supramolecules.

Collectively, these evidence suggest that the supramolecules may become sufficiently stable to self-assemble without imposing a substantial strain on their components.[13b,15] The geometric stability of these macrocyclic molecules allows for their preservation in the crystal lattice. Because large cyclic coordination molecules may not form high-density close-packed structures, they may be prone to form porous crystalline solids with open pores available for gas absorption and guest inclusion.[16] However, the expected diversity of the conceivable arrangements of the coordination rings to shape the pore geometries and form porous materials and coordination polymers remains remains largely unexplored.[17]

The scope of the present investigation was to modulate the structuring of coordination cyclic supramolecules into porous crystalline materials and coordination polymers by the systematic variation of the lateral substituents of the scorpionate ligand based on the bis-pyrazole system extended with a thioether function and the Ag(I) ion, as shown in Figure 1.[11,18] The metal nodes of the supramolecules, capable of dictating the generation of hexameric cyclic coordination supramolecules, interact through anions, producing a capsular tetrahedron, whose repetition in the crystal lattice yields two types of cavities, one at the interior of the capsule and the other formed by the packing of the capsules themselves (Figure 1b). The cavity size and the polarity of the intracapsular space was tailored by the systematic variation of the peripheral aromatic moiety of the ligand by incorporating methyl-phenyl, naphthyl, methoxy-phenyl, and fluoro-phenyl groups (L^{SNf}, L^{SPhOMe}, $L^{SPhm\text{-}Me}$, $L^{SPhp\text{-}Me}$, and L^{SPhF}, Figure 1a). Moreover, we investigated how the symmetry and the interactions of the anions tune the connectivity of the supramolecules by studying the effect of $CF_3SO_3^-$ and PF_6^- on the overall structural arrangement from polymeric (nonporous) to porous macrocyclic products. It can be anticipated that the presence of the symmetric PF_6^- anions and the ligand preorganization guarantees the formation of the capsular reticular structure; hence, the pore capacity and the gas-sorption properties can be controlled by the rational choice of the ligand.

The porosity of the compounds was investigated by performing gas adsorption measurements of the gases of interest for industrial and medical applications, such as CO_2, CH_4, N_2 and N_2O, showing interesting performances and

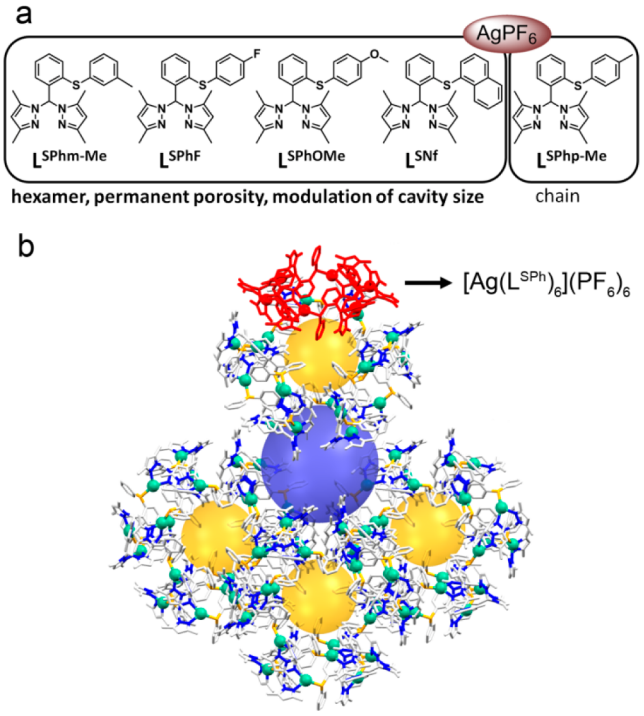

Figure 1. (a) Ligands used to prepare the microporous crystals with $AgPF_6$ discussed in this study. (b) Depiction of the arrangement of the hexameric unit (in red) into a porous material characterized by two types of cavities (blue and yellow spheres). The silver atoms are depicted as green spheres.[11]

selectivity of the material toward carbon dioxide vs nitrogen. The effective gas capture by the novel microporous materials allowed a direct spectroscopic observation of the gas molecules absorbed in the microporous crystals in intimate contact with the supramolecules. The 2D $^1H-^{13}C$ magic angle spinning NMR performed on the samples loaded with enriched $^{13}CO_2$ could establish the stable gas inclusion in the pores and the gas distribution between the intra- and intercavities.[19]

Our results contribute to the understanding of how the coordination polymers aggregate into infinite length linear chains or, alternatively, how they form stable oligomeric rings for the simultaneous contributions of several factors, including the nature of the anion. The dominance of the ionic interactions considerably differentiates the proposed structures and their chemical behavior from the infinite metal–organic lattice of the metal organic frameworks (MOF), stimulating the development of parallel fields of exploration on the influence of various-rank interactions to build metal–organic molecular architectures.

EXPERIMENTAL SECTION

Bis(3,5-dimethylpyrazolyl)ketone was prepared as reported in the literature,[20] and the aldehydes were prepared by a slight modification of a procedure reported in the literature.[21] All of the other reagents and solvents were commercially available (Sigma-Aldrich). The ^1H NMR spectra were recorded on a Bruker Avance 300 spectrometer using standard Bruker pulse sequences. The chemical shifts are reported in parts per million (ppm), referenced to residual solvent protons. The infrared spectra were recorded from 4000 to 700 cm^{-1} on a PerkinElmer FTIR Nexus spectrometer equipped with a Smart Orbit HATR accessory (diamond crystal). The elemental analyses (C, H, and N) were performed with a Carlo Erba EA 1108 automated analyzer. Details on the synthesis and characterization of the ligands

dx.doi.org/10.1021/ja507555j | J. Am. Chem. Soc. 2014, 136, 14883–14895

L^{SNf}, $L^{SPhm\text{-}Me}$, $L^{SPhp\text{-}Me}$, L^{SPhF}, and L^{SPhOMe} and of the silver complexes with $AgPF_6$ and $AgCF_3SO_3$ are provided in the Supporting Information.

X-ray Crystallography. The single-crystal data were collected on Bruker Smart 1000 and Bruker Smart APEXII area-detector diffractometers (Mo Kα; λ = 0.71073 Å). The cell parameters were refined from the observed setting angles and the detector positions of selected strong reflections. The intensities were integrated from several series of exposure frames that covered the sphere of the reciprocal space.[22] A multiscan absorption correction was applied to the data using the program SADABS.[23] The structures were solved by direct methods (SIR97[24] and SIR2004[25]) and refined with full-matrix least-squares (SHELXL-97),[26] using the Wingx software package.[27] In the $[Ag(L^{SNf})]_6(PF_6)_6$, $[Ag(L^{SPhm\text{-}Me})]_6(PF_6)_6$, $[Ag(L^{SPhF})]_6(PF_6)_6$, and $[Ag(L^{SPhOMe})]_6(PF_6)_6$ complexes, the solvent was treated using the PLATON/SQUEEZE program.[28] The yield of crystallization varied from more than 80% for $[Ag(L^{SNf})]_6(PF_6)_6$ and $[Ag(L^{SPhm\text{-}Me})]_6(PF_6)_6$ to approximately 20% for $[Ag(L^{SPhOMe})]_6(PF_6)_6$ and $[Ag(L^{SPhF})]_6(PF_6)_6$. Graphical material was prepared with the Mercury 3.0[29] program. CCDC 1014232−1014242 contains the supplementary crystallographic data for this study.

Hirshfeld Surface Analysis. The Hirshfeld surface (HS) properties were investigated to gain a thorough description of the interactions occurring between the peripheral and differently functionalized aromatic rings in the hexamers and in the coordination polymeric chains and of the interactions occurring between the anions (PF_6^- and $CF_3SO_3^-$) and the surrounding molecules.[30] The HS defines the volume of space in a crystal in which the sum of the electron density of the spherical atoms for the molecule (promolecule) exceeds that for the crystal (procrystal). The HS property is defined by the following expression:

$$w(r) = \frac{\sum_{i\in \text{molecule}} \rho_i^{\text{atom}}(r)}{\sum_{i\in \text{crystal}} \rho_i^{\text{atom}}(r)} = \frac{\rho_{\text{promolecule}}}{\rho_{\text{procrystal}}}$$

The $w(r)$ value of 0.5 isosurface enveloping the molecule corresponds to the HS, which contains a region of space in which the promolecule electron density is greater than that of the surrounding molecules.

Various properties of the HS can be computed and visualized, particularly, d_e and d_i, which represent the distance from a point on the surface to the nearest nucleus outside or inside the surface, respectively. The d_{norm} is the normalized contact distance and is defined by considering d_e and d_i and the van der Waals radii of the atoms, as given in the following equation:

$$d_{\text{norm}} = \frac{d_i - r_i^{\text{vdW}}}{r_i^{\text{vdW}}} + \frac{d_e - r_e^{\text{vdW}}}{r_e^{\text{vdW}}}$$

Mapping d_{norm} on the HS provides a clear and thorough picture of the interactions occurring between the adjacent molecules or the molecular fragments that are shorter than the sum of the van der Waals radii (visualized as red spots on the HS). The HS surface and its properties were calculated using the CrystalExplorer 3.1 program.[31] Certain crystal structures were characterized by the presence of disordered fragments. During the HS analysis, these fragments were considered with their fractional occupancies.[30a]

X-ray Powder Diffraction. The powder XRD patterns were collected using a Thermo ARL X'tra powder diffractometer (Cu Kα radiation) equipped with a Thermo Electron solid state detector. The data collection was performed in a Bragg−Brentano configuration using 0.05° steps with a counting time ranging from 1 to 5 s. Temperature-dependent experiments were performed using an Anton Paar TTK450 chamber connected to a vacuum apparatus. Prior to the measurements, the crystalline material was subjected to thermal treatment at 60 °C under a vacuum for 2 h to completely remove the residual volatile component in the cavities derived from the solvent of crystallization.

Gas Sorption Meaurements. Carbon dioxide, methane, nitrous oxide and nitrogen adsorption−desorption isotherms for the porous materials were performed at 195, 273, and 298 K using a Micromeritics analyzer ASAP 2050 (up to 10 atm) and a Micromeritics analyzer ASAP 2020 (up to 1 atm). The samples were previously outgassed overnight at 110 °C.

Solid State NMR. The ^{13}C solid state NMR was run at 75.5 MHz on a Bruker Avance 300 instrument operating at a static field of 7.04 T equipped with a 4 mm double resonance MAS probe. The samples were spun at the magic angle at a spinning speed of 12.5 kHz, and the ramped amplitude cross-polarization (RAMP-CP) transfer of magnetization was applied. The 90° pulse for the proton was 2.9 μs. The ^{13}C cross-polarization (CP) MAS experiments were run using a recycle delay of 10 s and a contact time of 2 ms. Phase-modulated Lee−Goldburg (PMLG) heteronuclear $^1H-^{13}C$ correlation (HETCOR) experiments coupled with fast magic angle spinning allowed the recording of the 2D spectra with a high resolution in the hydrogen and in the carbon dimensions. Narrow hydrogen resonances, with line widths on the order of 1−2 ppm, were obtained with homonuclear decoupling during t_1; this resolution permits a sufficiently accurate determination of the proton species present in the system. The 2D PMLG $^1H-^{13}C$ HETCOR spectra were run with an LG period of 18.9 μs. The efficient transfer of magnetization to the carbon nuclei was performed by applying the RAMP-CP sequence. The cross-polarization times of 50 μs, 0.5, 1, and 5 ms were applied. Quadrature detection in t_1 was achieved by the time proportional phase increments method (TPPI). The carbon signals were acquired during t_2 under proton decoupling by applying the two-pulse phase modulation scheme (TPPM). The 2D experiments were conducted at 298 and 240 K under magic-angle spinning (MAS) conditions at 12.5 kHz and 8 kHz, respectively.

The ^1H MAS NMR measurements were performed on a Bruker Avance III 600 MHz instrument operating at 14.1 T using the windowed phase modulated Lee-Goldbug decoupling sequences (*w*PMLG) to improve the ^1H resolution. A MAS Bruker probe head was used with 2.5 mm ZrO_2 rotors spinning at the speed of 13.6 kHz and an RF power of 86 kHz, calibrated by a nutation experiment on adamantane. The *w*PMLG was used with an acquisition window of 3.9 μs, a pulse length of 0.7 μs and an interpulse delay of 0.1 μs.

RESULTS AND DISCUSSION

The synthesis of the ligands is described in Scheme 1. The ligands L^{SNf}, L^{SPhOMe}, $L^{SPhm\text{-}Me}$, $L^{SPhp\text{-}Me}$, and L^{SPhF} were prepared by treating bis(3,5-dimethylpyrazolyl)ketone and the appropriate aldehydes using $CoCl_2$ hydrate as a catalyst. The silver complexes were easily prepared by treating equimolar amounts of ligands and $AgPF_6$ or $AgCF_3SO_3$ to investigate the

Scheme 1. Ligand Synthesis

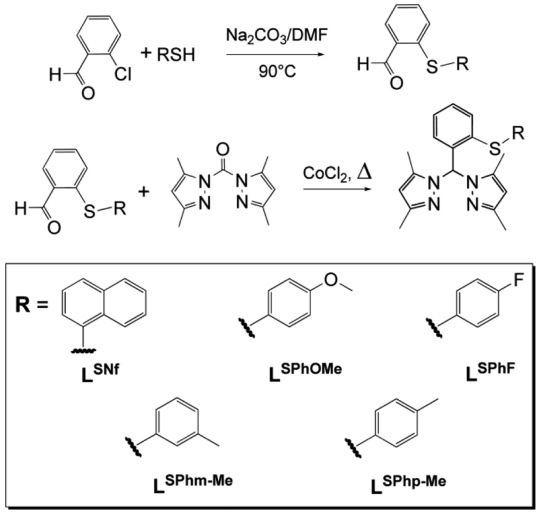

dx.doi.org/10.1021/ja507555j | J. Am. Chem. Soc. 2014, 136, 14883−14895

role of the counterion in the resulting structural arrangement.[12] The porous crystals having a cubic phase (with PF_6^-) were obtained by crystallization in various solvent mixtures (such as acetone/diethyl ether or dichloromethane/hexane), and their porosity was tested with gas adsorption measurements. The coordination polymeric chains obtained with the triflate anion were obtained by the recrystallization of the powder in various solvent mixtures, namely, dichloromethane/hexane, acetone/diethyl ether, and THF/hexane.

Molecular Structures with the PF_6^- Anion. When using the PF_6^- anion, the hexameric supramolecular structures $[Ag(L)]_6(PF_6)_6$ are preferentially obtained (Figure 2). The complexes $[Ag(L^{SNf})]_6(PF_6)_6$, $[Ag(L^{SPhOMe})]_6(PF_6)_6$, $[Ag(L^{SPhm\text{-}Me})]_6(PF_6)_6$, and $[Ag(L^{SPhF})]_6(PF_6)_6$ are isostructural, and the only exception is represented by the system with the $L^{SPhp\text{-}Me}$ ligand that forms a coordination polymeric chain analogous to that found for the complexes with the triflate anion, which will be described later (see Figure 6).

In all of the hexameric complexes, the ligand acts as a N_2 bidentate on a metal and bridges on another silver atom with the thioether group, whereas the central phenyl ring adopts a particularly fixed geometry (Figures S1 and S2, Supporting Information).[32] The peripheral phenyl ring is located above one of the pyrazole rings, giving rise to a weak $\pi-\pi$ interaction. The pyrazole rings of six ligands define the exteriors of the hexamer, whereas the peripheral aromatic rings are oriented toward the interior. The cyclic hexameric molecular structures exhibit a pore in the central part whose size is modulated by the encumbrance of the substituents. Pore sizes of 1.6, 2.6, and 3.0 Å were measured for the $[Ag(L^{SNf})]_6(PF_6)_6$, $[Ag(L^{SPhm\text{-}Me})]_6(PF_6)_6$, and $[Ag(L^{SPhF})]_6(PF_6)_6$ complexes, respectively. In the $[Ag(L^{SPhOMe})]_6(PF_6)_6$ complex, the methoxy groups occlude the intraring space (Figure 2). The cyclic hexamers form cubic crystal structures, in which the PF_6^- anion exhibits a fragmented site occupation; per each silver cation of the asymmetric unit, the PF_6^- anion is distributed in three positions in the unit cell as follows: (1) a 0.1666 fraction lying on a ternary axis and on an inversion center, (2) a 0.3333 fraction lying on a ternary axis, and (3) a 0.5 fraction lying on a binary axis. This latter fraction links two silver atoms of the symmetry-related hexamers such that the centroids of four hexamers occupy the vertex of a tetrahedron.

The four cyclic hexamers self-assemble, forming a capsule with a highly symmetric Platonic shape (tetrahedron), which results in an intracapsular space. The packing of the capsules forms a network of interconnected cavities (intercapsular space) (Figure 3). The intercapsular cavities have a size of approximately 14 Å in diameter, as described by a spherical approximation, while the size of the intracapsular cavities is modulated by the steric encumbrance of the peripheral substituents (diameter of 5 and 11 Å in $[Ag(L^{SNf})]_6(PF_6)_6$ and $[Ag(L^{SPhm\text{-}Me})]_6(PF_6)_6$, respectively).

The distance between the fluorine of PF_6^- and the silver atoms varies over the range of 2.749(3)-2.818(9) Å, suggesting the weak nature of this interaction (Table S4, Supporting Information). The PF_6^- anion, which acts as a linker between the metals, is also immobilized by a C−H···F interaction with one of the methyl groups of the pyrazole ring. A pictorial view of the environment surrounding the different types of PF_6^- anions can be appreciated by inspecting the d_{norm} mapped on the HS reported in Figure 4 for the $[Ag(L^{SNf})]_6(PF_6)_6$ complex as representative of the four compounds.

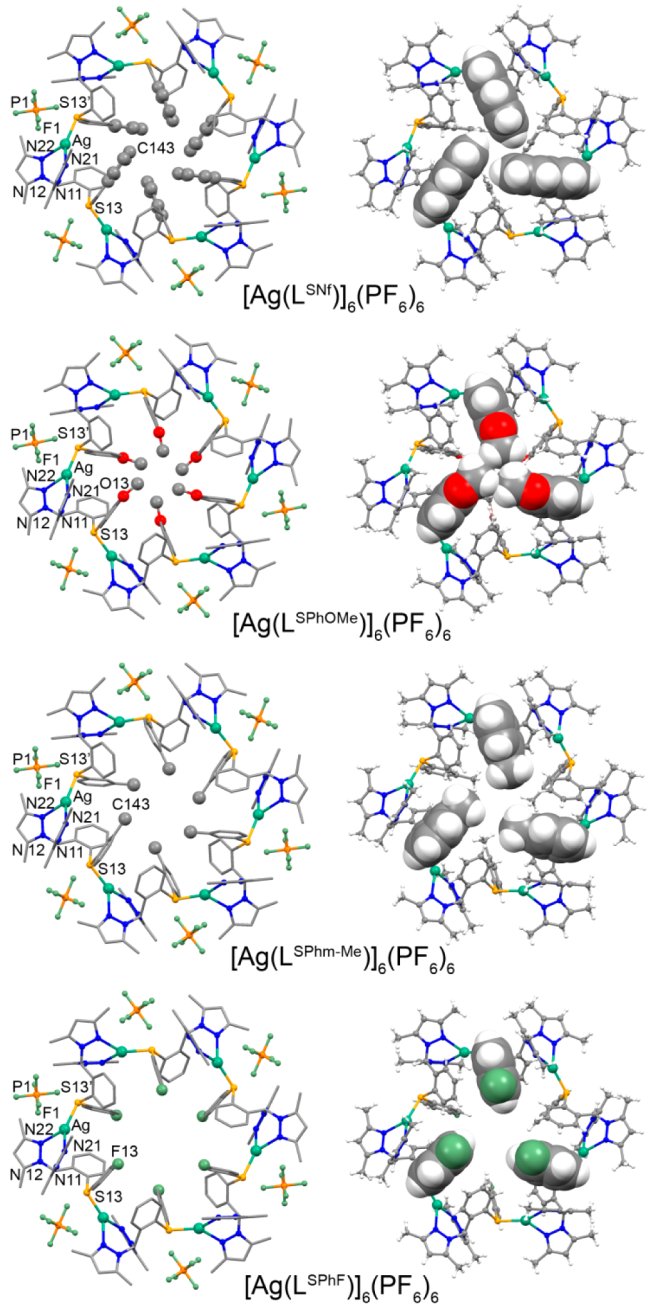

Figure 2. Left, the molecular structures of the hexameric unit of $[Ag(L^{SNf})]_6(PF_6)_6$, $[Ag(L^{SPhOMe})]_6(PF_6)_6$, $[Ag(L^{SPhm\text{-}Me})]_6(PF_6)_6$, and $[Ag(L^{SPhF})]_6(PF_6)_6$. The hydrogen atoms are omitted for clarity. The prime (′) symbol denotes the symmetry-related atoms. Right, representation of the different sizes of the pores for the hexameric complexes. The peripheral aromatic groups are depicted with the van deer Waals atomic radii. Colors: Ag, green; S, yellow; N, blue; C, gray; O, red; F, light green; P, orange.

In addition, a thorough depiction of the interaction exchanged by the three types of PF_6^- anions could be obtained by inspecting the fingerprint plots, which are 2D diagrams that provide a clear indication of the subtle differences between the similar structural arrangements, as reported in Figure 5 and in Figure S3 (Supporting Information). It is evident that the anion that acts as a linker between the silver cations exhibits the most conserved intermolecular contacts because the surrounding environment is identical in the four compounds and the

dx.doi.org/10.1021/ja507555j | J. Am. Chem. Soc. 2014, 136, 14883−14895

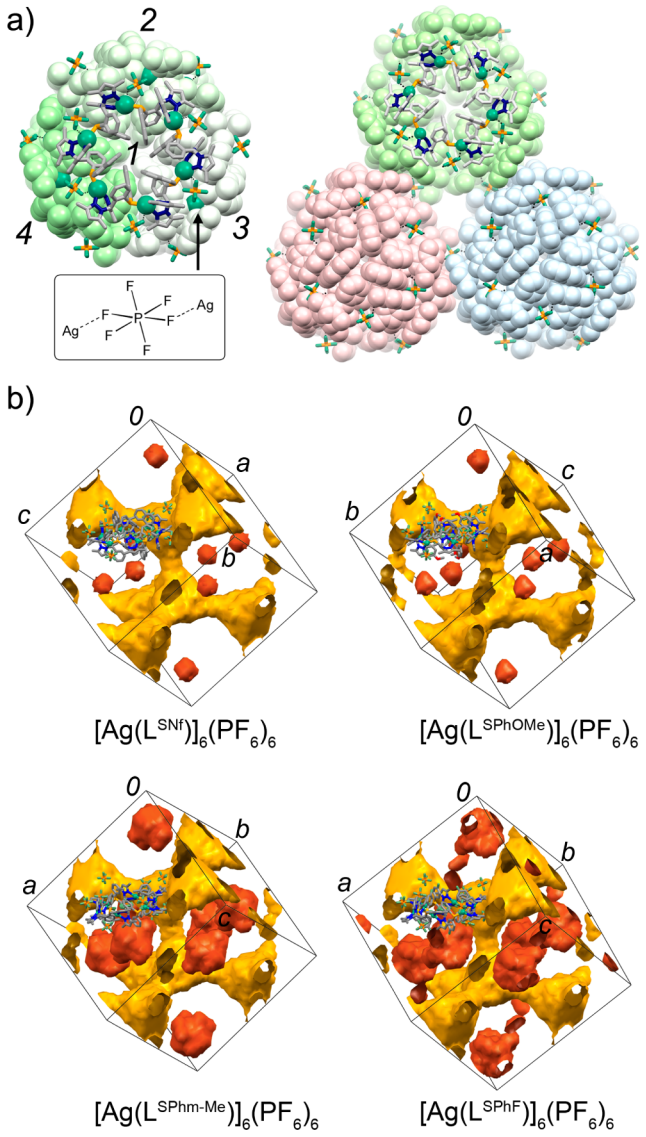

Figure 3. (a) Assembly of the capsule by four hexamers, right, and capsular packing, left. (b) Depiction of the two types of cavities in the crystal structures. Yellow: intercapsular space; red: intracapsular space. The cavities were generated by rolling a probe sphere of a 3.2 Å diameter on the surface of the cavities.

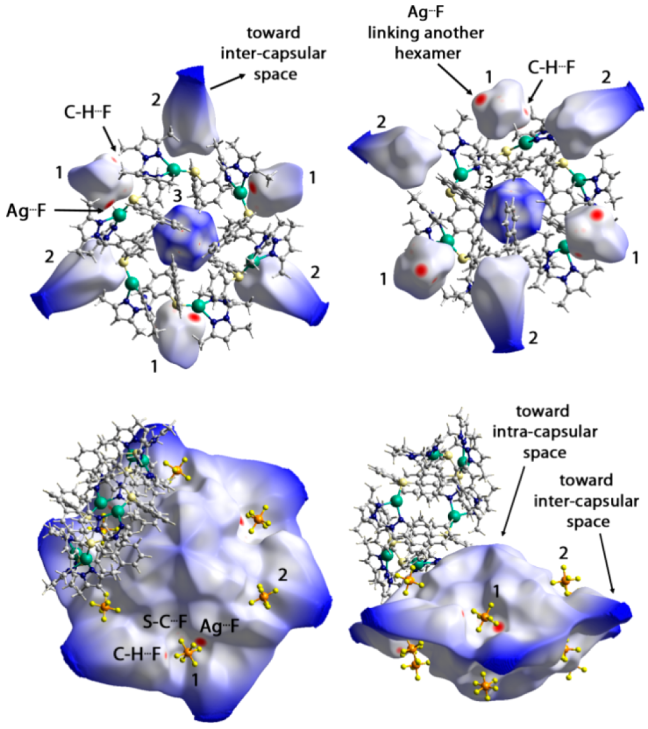

Figure 4. Above, depiction of the d_{norm} mapped on the Hirshfeld surface (grades of blue) of the three types of PF_6^- anions for the representative complex $[Ag(L^{SNf})]_6(PF_6)_6$. A ball and stick representation is shown for one hexamer, and the surrounding molecules were omitted for clarity (above left, top view and above right, bottom view). Below, depiction of the d_{norm} mapped on the Hirshfeld surface for one hexamer of $[Ag(L^{SNf})]_6(PF_6)_6$. One out of four hexamers defining a capsule and the connecting PF_6^- anions are shown with the ball and stick representation, and the remaining molecules were omitted for clarity.

fingerprint plots are nearly superimposable. In contrast, the third type of PF_6^- exhibits different types of interactions with the hexamers, which is in agreement with its position within the structure. This anion is embedded into the hexamer and exchanges contacts with the differently functionalized peripheral phenyl groups of the ligand. The second type of PF_6^- exhibits moderately conserved interactions among the four structures, according to the similar fingerprint plots (see Figure S3, Supporting Information). This result is in agreement with the location of this anion in a pocket formed by three hexamers and lined with pyrazole and phenyl rings. A portion of the surface of this anion is also pointing toward the intercapsular cavity (see Figure 4).

The HS of the hexameric assemblies shows that each hexamer is connected with two intracapsular spaces and is in communication with six intercapsular cavities (Figures 4 and S4, Supporting Information). Both of the 3D cavities are filled by highly disordered solvent molecules, which could not be properly located by the difference Fourier map. The solvent can be easily removed without loss of crystallinity, resulting in porous crystalline structures. The empty total volume diminishes as the bulkiness of the substituent of the aromatic ring increases, and the following order is observed: $[Ag(L^{SNf})]_6(PF_6)_6 \approx [Ag(L^{SPhOMe})]_6(PF_6)_6 < [Ag(L^{SPhm-Me})]_6(PF_6)_6 \approx [Ag(L^{SPhF})]_6(PF_6)_6$ (Table 1).[33] The substituents on the peripheral phenyl ring affects the size of the intracapsular space, thus the increasing bulkiness of substituents from F, *m*-Me, OMe, to Nf determines the shrinkage of this cavity type. In contrast, the cavity size of the intercapsular space is lined with methyl groups of the pyrazole rings and is nearly invariant in the four structures (see Table 1).

Molecular Structures with the $CF_3SO_3^-$ Anion. When employing the triflate anion, the silver complexes crystallize in the form of coordination polymeric chains, and the general formula is $[Ag(L)]_n(CF_3SO_3)_n$ (Figure 6). As stated above, when mixing $AgPF_6$ with the ligand $L^{SPhp-Me}$, the molecular structure of the complex presents structural features analogous to those obtained with the triflate anion. The molecular arrangement in $[Ag(L^{SNf})]_n(CF_3SO_3)_n$, $[Ag(L^{SPhOMe})]_n(CF_3SO_3)_n$, $[Ag(L^{SPhm-Me})]_n(CF_3SO_3)_n$, $[Ag(L^{SPhp-Me})]_n(CF_3SO_3)_n$, and $[Ag(L^{SPhp-Me})]_n(PF_6)_n$ are similar, even though these complexes crystallize in different space groups (see Experimental Section); therefore, their structures will be described together. As reported for the structures with the PF_6^- anions, the ligand acts as a N_2 bidentate on a metal

dx.doi.org/10.1021/ja507555j | J. Am. Chem. Soc. 2014, 136, 14883−14895

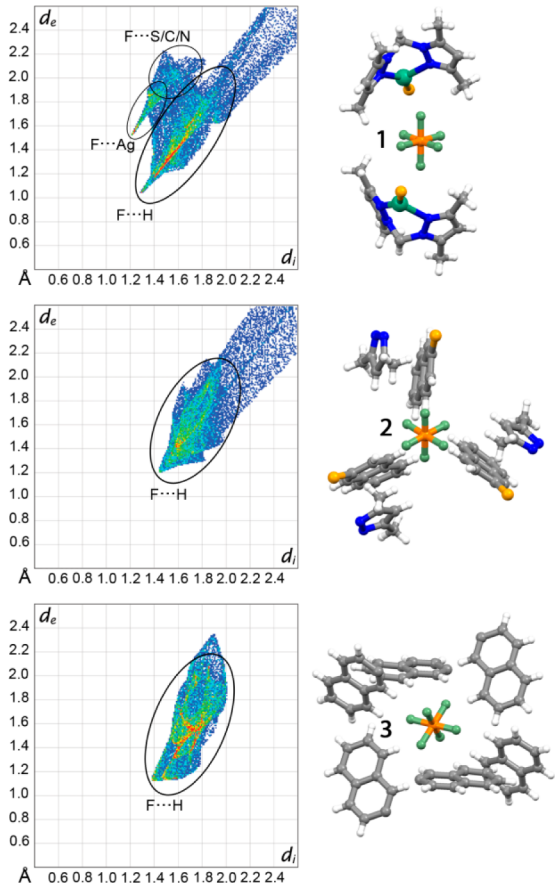

Figure 5. Fingerprint plots of the three types of PF_6^- anions in $[Ag(L^{SNf})]_6(PF_6)_6$ along with a ball and stick representation of their packing environment; d_e and d_i represent the distance from the Hirshfeld surface to the nearest nucleus outside or inside, repectively, the surface (see Experimental Section). Color codes varying from blue to red highlights the frequency with which a (d_e, d_i) is observed.

and bridges on another silver atom with the thioether group and with the central phenyl ring in a rigid geometry (Figures S1 and S2, Supporting Information). In contrast to the structures of the hexameric complexes, the peripheral phenyl ring exhibits a higher degree of conformational flexibility because it is not consistently stacked above one of the pyrazole rings, as occurs in the hexameric complexes.[32] When viewing the coordination polymeric chains of $[Ag(L^{SNf})]_n(CF_3SO_3)_n$, $[Ag(L^{SPhOMe})]_n(CF_3SO_3)_n$, $[Ag(L^{SPhm\text{-}Me})]_n(CF_3SO_3)_n$, $[Ag(L^{SPhp\text{-}Me})]_n(CF_3SO_3)_n$, and $[Ag(L^{SPhp\text{-}Me})]_n(PF_6)_n$ along their direction of propagation (Figure 6), it can be appreciated that their projection has a square section with the sides in the 18.9–14.4 Å range. The larger size belongs to $[Ag(L^{SNf})]_n(CF_3SO_3)_n$, which presents the most cumbersome substituent, namely the naphthyl residue. These chains exhibit a helical arrangement with a pitch over the range of 20.5–23.0 Å that comprise four AgL units. The exterior of the chains is defined by alternate anions and pyrazole rings, whereas the peripheral aromatic moieties are located in the interior. This arrangement is a structural feature that also characterizes the hexameric complexes, although in the coordination polymeric chains, there is a less defined orientation of the anions that surround the chains. In the hexameric complexes, the PF_6^- moiety occupies precise and invariant structural sites for all of the complexes, whereas in the chains, the anions interact with the metals but are free to rotate around the Ag–O bond. This result can be evidenced in the more varied shape of the fingerprint plots for the structures of the chain-like complexes (Figures S5–S10, Supporting Information) compared with those of the hexamers (Figure S3, Supporting Information). From an aesthetic viewpoint, the hexameric species can be imagined as derived by a slight twisting reorientation of a fraction of the chains comprising six AgL units.

The $[Ag(L^{SPhF})]_n(CF_3SO_3)_n$ complex crystallizes as a coordination polymeric chain, but the structural features are different from the previously described structures; the silver atoms are organized in a zigzag fashion, and the polymer does not form a helix. In addition, by inspecting its projection along the propagation of the molecule, it can be observed that the –PhF group and one of the pyrazole rings are oriented on one side, whereas the central phenyl ring and the triflate anion are located on the other side of the chain.

Supramolecular Isomerism. The role played by the symmetry and the interactions exchanged by the counteranions (BF_4^-, PF_6^-, $CF_3SO_3^-$, and NO_3^-) and Ag(I) in the presence of the L^{SPh} ligand has been previously investigated and was capable of dictating the assembly of cyclic coordination supramolecules into two different porous periodic lattices. The presence of the highly symmetric BF_4^-, PF_6^- anions acted as a link between the cyclic supramolecules, forming a robust structure exhibiting permanent porosity (see Figure 1b).[11] Hence, with L^{SPh}, the determinant for the 3D arrangement was the anion, but the hexameric building block was an invariant feature. In the present case, the modification of the peripheral phenyl ring with the introduction of various substituents implies that with the less symmetric $CF_3SO_3^-$ anion, the hexameric units are no longer observed; instead, coordination polymeric chains are preferentially formed. However, the presence of the PF_6^- anion is associated with the generation of four hexameric systems out of five complexes, and this may be because of the high symmetry of the anion that can be accommodated in the highly symmetric cubic structure. In fact, the octahedral symmetry of PF_6^- makes it a good candidate to occupy highly symmetric positions within the cubic lattice. In the case of L^{SPhOMe} and L^{SPhNf} along with the easily identifiable crystals of the cubic form, a small fraction of prismatic crystals of the coordination polymeric chain was isolated, and the molecular structure of $[Ag(L^{SPhOMe})]_n(PF_6)_n$ is reported in Figure 6. This result implies that it may be possible, under specific conditions, to drive the crystallization process toward one (chain) or the other (hexamer) molecular organization. As

Table 1. Volume of the Cavities[a] (Å^3) Per Unit Cell of the Four Hexameric Structures[b]

	$[Ag(L^{SNf})]_6(PF_6)_6$	$[Ag(L^{SPhOMe})]_6(PF_6)_6$	$[Ag(L^{SPhm\text{-}Me})]_6(PF_6)_6$	$[Ag(L^{SPhF})]_6(PF_6)_6$
total	11488 (14.4)	12688 (16.0)	18108 (22.3)	17248 (21.6)
intracapsular space	586 (0.7)	857 (1.1)	5839 (7.2)	5711 (7.2)
intercapsular space	10902 (13.7)	11831 (14.9)	12269 (15.1)	11537 (14.4)

[a]Probe radius 1.6 Å, grid 0.7 Å [b]The % of the volume of the cavities with respect to the unit cell volume is reported in the parentheses.

dx.doi.org/10.1021/ja507555j | J. Am. Chem. Soc. 2014, 136, 14883–14895

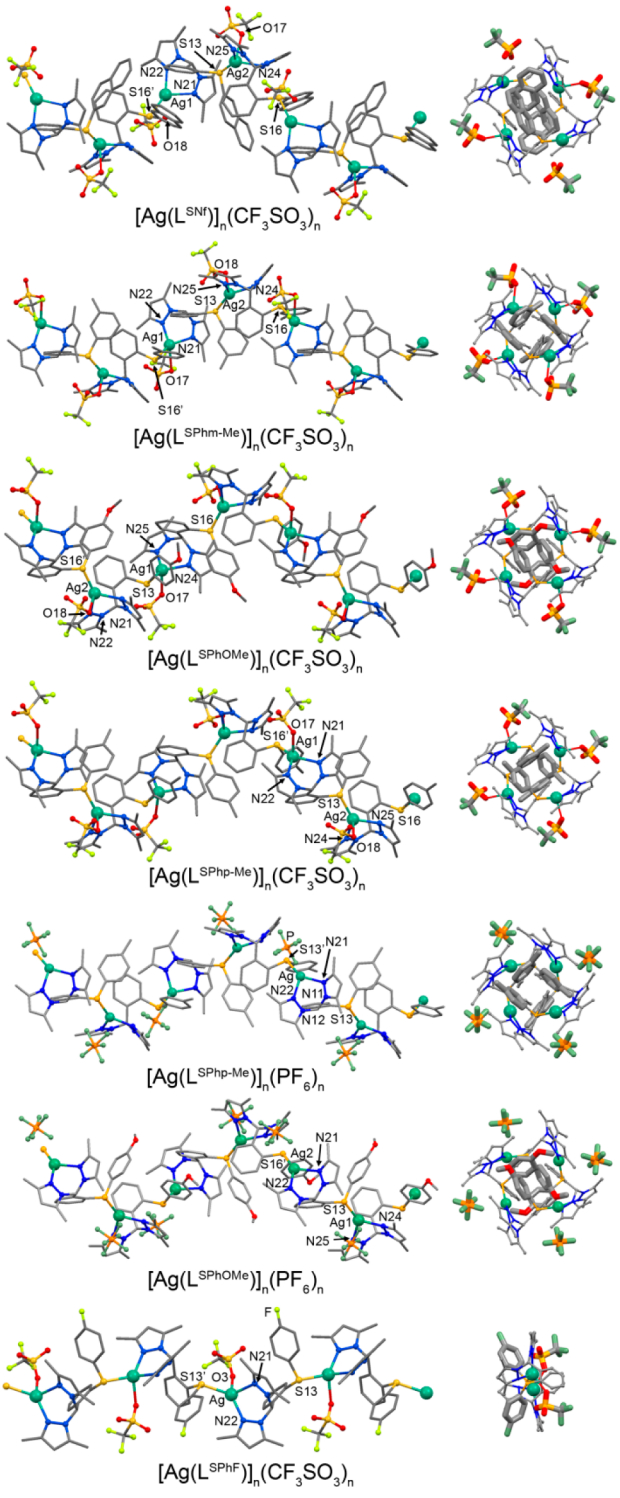

Figure 6. A portion of the coordination polymeric chains of $[Ag(L^{SNf})]_n(CF_3SO_3)_n$, $[Ag(L^{SPhOMe})]_n(CF_3SO_3)_n$, $[Ag(L^{SPhm\text{-}Me})]_n(CF_3SO_3)_n$, $[Ag(L^{SPhp\text{-}Me})]_n(CF_3SO_3)_n$, $[Ag(L^{SPhp\text{-}Me})]_n(PF_6)_n$, $[Ag(L^{SPhOMe})]_n(PF_6)_n$, and $[Ag(L^{SPhF})]_n(CF_3SO_3)_n$. Side views along with a depiction of the chains viewed along the direction of propagation of the helix. The thick stick representation highlights the anions and the peripheral aromatic moieties of the ligand. The prime (′) symbol denotes the symmetry-related atoms. Colors: Ag, green; S, yellow; N, blue; C, gray; O, red; F, light green; P, orange.

stated above, there are remarkable similarities between the molecular organization of the AgL fragments in the chain and in the hexameric systems, a situation that has been previously documented for other silver coordination polymers.[34] In a simplified description, one can imagine the chains as being derived by the polymerization of hexamers. This process would ideally require the rupture and formation of coordination bonds so that the two structural arrangements can be defined as supramolecular isomers.[35] The crystallization conditions play a decisive role in directing the structural type that can be obtained;[34,36] therefore, we tested several crystallization conditions by changing the concentration of the samples while maintaining the metal/ligand/anion ratio of 1/1/1. In a diluted solution, we could recover large crystals with an octahedral shape corresponding to the hexamers crystallizing in the cubic $Fd\bar{3}$ space group. However, when increasing the concentration of the sample, a certain amount of prismatic crystals of the coordination polymeric chain cocrystallized with a large amount of microcrystals of the cubic phase. This behavior could be reproduced for the systems comprising the L^{SNf} and L^{SPhOMe} ligands, whereas $L^{SPhm\text{-}Me}$ consistently gave cubic phase crystals in all of the concentration conditions tested. In contrast, $L^{SPhp\text{-}Me}$ consistently produced prismatic crystals corresponding to the coordination polymeric chain. The reason for this behavior can be explained by inspecting the environment surrounding the peripheral aromatic moieties in the structures of the four hexameric complexes and in the structure of the model hexameric complex $[Ag(L^{SPhp\text{-}Me})]_6^{6+}$. This model complex was generated by adding a methyl residue to the parent compound $[Ag(L^{SPh})]_6(PF_6)_6$. In Figure S11 (Supporting Information), it can be observed that for *model*-$[Ag(L^{SPhp\text{-}Me})]_6^{6+}$, there is a considerable steric hindrance between the *p*-Me residues of the adjacent hexameric units, thus hindering its assembly in favor of the more sterically relaxed chain-like structure. In the other hexameric complexes, the peripheral groups are sufficiently separated to be detrimental to the formation of the cubic structure, which is the preferred phase. The occurrence of the coordination polymeric chains with L^{SNf} and L^{SPhOMe} but not with $L^{SPhm\text{-}Me}$ can be therefore associated with the bulkiness of the peripheral aromatic group. In fact, by inspecting the hexameric unit, the steric hindrance toward the center of the pore (see Figure 2) varies in the order $[Ag(L^{SPhOMe})]_6(PF_6)_6 \approx [Ag(L^{SNf})]_6(PF_6)_6$, $> [Ag(L^{SPhm\text{-}Me})]_6(PF_6)_6$, $\approx [Ag(L^{SPhF})]_6(PF_6)_6$. This implies the bulkier aromatic moieties are more prone to give rise to coordination polymeric chain, hence supramolecular isomers, in which there are no unfavorable interactions between the peripheral aromatic moieties.

Characterization and Stability of the Microcrystalline Material. Powder X-ray diffraction (PXRD) was employed to characterize all of the material that was obtained after the crystallization procedures. Although the cubic phase crystals of the hexameric species were easily identifiable in the crystallizing flasks by optical microscopy, the material was analyzed with powder X-ray diffraction to determine its purity and to rule out the possible contamination with prismatic crystals. The experimental profiles were compared with the theoretical profiles derived by the single-crystal X-ray characterization and demonstrated the exclusive formation of the cubic crystal structures. PXRD was also employed to gain insights into the thermal stability and structural response of the crystalline material of $[Ag(L^{SPhm\text{-}Me})]_6(PF_6)_6$ and $[Ag(L^{SNf})]_6(PF_6)_6$ in the presence of external stimuli, such as vacuum, volatile

dx.doi.org/10.1021/ja507555j | J. Am. Chem. Soc. 2014, 136, 14883−14895

components that can be trapped into the cavities, and water. Both of the complexes maintain a long-range structural order up to 180 °C and without any phase transition (Figures S12 and S13, Supporting Information). When the pre-evacuated crystalline material was exposed to saturated acetone vapors, a noticeable shift of all of the diffraction peaks at lower 2θ values occurred, implying a unit cell enlargement during the vapor sorption (Figure 7). It can be estimated that the unit cell

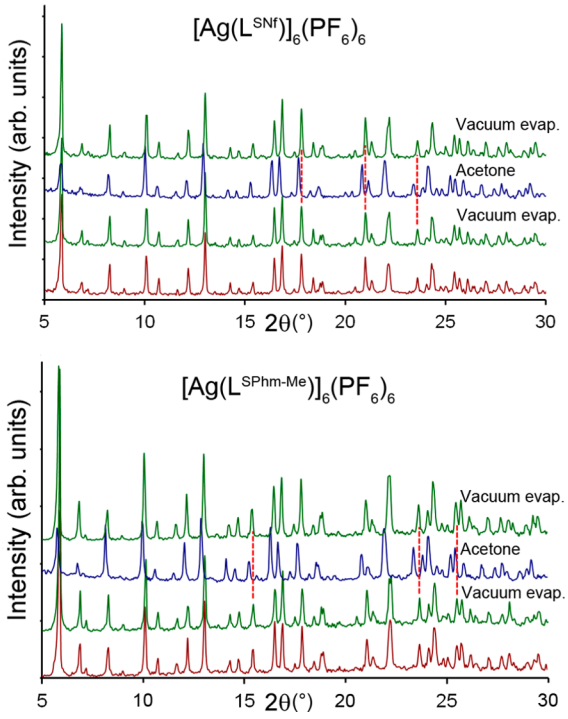

Figure 7. PXRD pattern showing the effect of the solvent absorption on the $[Ag(L^{SNf})]_6(PF_6)_6$ and $[Ag(L^{SPhm\text{-}Me})]_6(PF_6)_6$ crystals. The freshly ground crystals are shown in red. The crystals subjected to a high vacuum and T = 60 °C for 2 h are shown in green. The evacuated crystals were then exposed to saturated acetone vapors and are shown in blue. Dashed lines were depicted to better appreciate the shifts of representative peaks upon absorption and removal of acetone.

experienced a size shift of approximately 3% in volume (for crystals exposed to an acetone pressure of 0.3 bar at 25 °C). This result demonstrates that the occupation of the cavities by the acetone vapors occurs, and the accessibility of the cavities to chemical species without destroying the structure. The phenomenon is reversible; upon removal of the guest species under a vacuum, the unit cell parameters are restored to the original values of the empty structure, proving the zeolitic nature of the material. Several cycles of vacuum followed by exposure to acetone vapor could be applied to the material without the loss of structural order. Moreover, $[Ag(L^{SPhm\text{-}Me})]_6(PF_6)_6$ and $[Ag(L^{SNf})]_6(PF_6)_6$ are insoluble in water and the crystals can be soaked in water without change of shape or morphology (Figure S16, Supporting Information). The stability with respect to water could be confirmed by performing PXRD on samples soaked in water for 2 h and recovered by filtration. The samples showed an unaltered diffraction pattern, Figures S14 and S15 (Supporting Information).

Gas Adsorption Isotherms of the Microporous 3D Structures. An accurate inspection of the microporous 3D architectures with the PF_6^- anion reveals that all of the compounds exhibit an intercapsular space of approximately the same size (10902−12269 Å^3 range, see Table 1), but $[Ag(L^{SNf})]_6(PF_6)_6$ and $[Ag(L^{SPhOMe})]_6(PF_6)_6$ have a comparable volume of the intracapsular cavities (586 Å^3 and 857 Å^3, respectively), whereas the intracapsular volume of $[Ag(L^{SPhm\text{-}Me})]_6(PF_6)_6$ is nearly equal to that of $[Ag(L^{SPhF})]_6(PF_6)_6$ (5839 Å^3 and 5711 Å^3, respectively) (Figure 6). Thus, a few samples, such as $[Ag(L^{SNf})]_6(PF_6)_6$ and $[Ag(L^{SPhm\text{-}Me})]_6(PF_6)_6$, were selected as representative of the family of porous crystalline structures, and their adsorption properties were investigated.

The adsorption isotherms of the CO_2, CH_4, N_2 and N_2O gases at different temperatures were collected to demonstrate the accessibility and open porosity of the intra- and/or intercapsular spaces and to explore their potential for gas capture. N_2 at 77K was not adsorbed for kinetic reasons. The CO_2 adsorption isotherms of $[Ag(L^{SNf})]_6(PF_6)_6$ and $[Ag(L^{SPhm\text{-}Me})]_6(PF_6)_6$ at 195 K show a Langmuir profile, demonstrating the microporosity of the crystalline materials (Figure 8). $Ag(L^{SPhm\text{-}Me})]_6(PF_6)_6$ exhibits a CO_2 uptake of 66

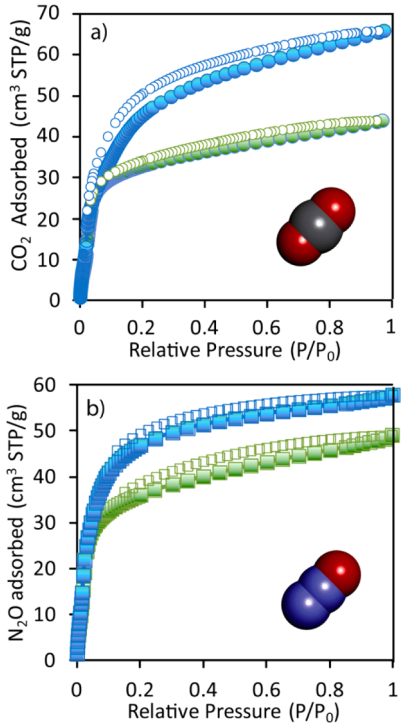

Figure 8. Adsorption/desorption isotherms for (a) CO_2 (circles) and (b) N_2O (squares) onto $Ag(L^{SPhm\text{-}Me})]_6(PF_6)_6$ (blue color) and $Ag(L^{SNf})]_6(PF_6)_6$ (green color) at 195 K.

cm^3/g (12.9 wt %) at 195 K and 1 bar, whereas at the same temperature, a lower value of 44 cm^3/g (8.6 wt %) was detected for $[Ag(L^{SNf})]_6(PF_6)_6$. This result is in agreement with the larger steric hindrance of the terminal naphthyl groups (with respect to the *m*-methylphenyl groups), which results in approximately a 37% decrease of the space available for the diffusion of the gas molecules. At 195 K and 1 bar, the CO_2 capacity corresponds to an occupied volume of 19879 Å^3 and 13576 Å^3 per unit cell for $[Ag(L^{SPhm\text{-}Me})]_6(PF_6)_6$ and $[Ag(L^{SNf})]_6(PF_6)_6$, respectively. By comparing these values with those calculated from the single crystal X-ray structures, it can be inferred that a complete filling of the intra- and

dx.doi.org/10.1021/ja507555j | J. Am. Chem. Soc. 2014, 136, 14883−14895

intercapsular spaces of the crystalline structures occurs. Per unit cell, 218 and 144 CO_2 molecules are arranged, respectively; i.e., up to 8 molecules can be hosted within a single capsule and 16 CO_2 molecules in each intercapsular cavity. Regarding the uptake values, these systems are effective in CO_2 capture, resulting in the adsorption of an amount comparable to that of the Ag-based imidazole frameworks recently described.[37] Moreover, in the porous supramolecular architectures, the adsorption isotherms of N_2O were also explored. The nitrous oxide N_2O isotherms exhibit Langmuir profiles, reaching plateau values of 58 and 49 $cm^3(STP)/g$ for $Ag(L^{SPhm\text{-}Me})]_6(PF_6)_6$ and $Ag(L^{SNf})]_6(PF_6)_6$, respectively. The adsorbed values are comparable to the maximum amount of CO_2 captured under the same temperature and pressure conditions, indicating a full loading of the pores.

Under the mild conditions of 298 and 273 K and up to 10 bar, the adsorption isotherms of CO_2 and CH_4 reveal that $[Ag(L^{SPhm\text{-}Me})]_6(PF_6)_6$ adsorbs a larger amount of CO_2 and CH_4 with respect to $[Ag(L^{SNf})]_6(PF_6)_6$. For example, at 298 K and 10 bar, $[Ag(L^{SPhm\text{-}Me})]_6(PF_6)_6$ adsorbs 36 and 22 $cm^3(STP)/g$ of CO_2 and CH_4, respectively, versus 26 and 13 $cm^3(STP)/g$ of $[Ag(L^{SNf})]_6(PF_6)_6$, respectively (Figure 9).

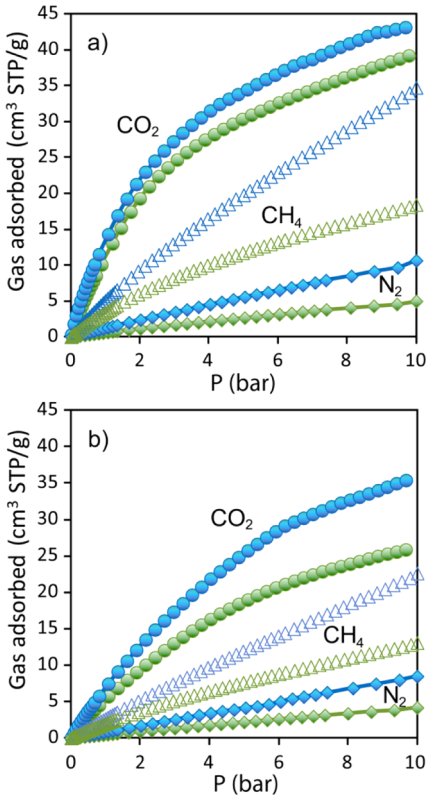

Figure 9. Adsorption isotherms CO_2 (filled circles), CH_4 (open triangles) and N_2 (filled diamonds) onto $Ag(L^{SPhm\text{-}Me})]_6(PF_6)_6$ (blue color) and $Ag(L^{SNf})]_6(PF_6)_6$ (green color) at 273 K (a) and 298 K (b).

Moreover, these materials preferably adsorb CO_2 over N_2 at room temperature and at 273 K. The N_2 adsorption isotherms, displayed in Figure 9, show a low uptake even at high pressures, and the amount is directly proportional to the pressure over the range up to 10 bar, indicating an extremely low affinity for nitrogen. This evidence can be favorably exploited for the selective absorption of carbon dioxide in a mixture with nitrogen. The selectivity of CO_2 vs N_2 binary mixtures was determined by the single-component isotherms using the ideal adsorbed solution theory (IAST), which has been successfully applied to predict the gas mixture separation by porous materials.[38] Under the mild conditions of low pressures and a temperature of 273 K, both of the compounds show a CO_2/N_2 selectivity of 14 starting from a CO_2/N_2 unbalanced mixture of 15:85, which is representative of industrial operative conditions (Figure S19, Supporting Information). In the absence of unsaturated metal sites or specific functional groups that could mainly interact with carbon dioxide (endowed with a quadrupole moment of -14.27×10^{-40} C m^2), the CO_2/N_2 selectivity is lower than that of the MOFs with unsaturated metal sites and site specificity but is comparable with other MOFs and zeolites.[39] Within the family of porous molecular materials they show a similar behavior and preferably adsorb CO_2 over N_2.[11,19,40]

The selectivity is associated with the isosteric heat of the CO_2 adsorption at low pressures, estimated as 25−27 kJ/mol, which is in agreement with the hydrophobic nature of the pyrazole methyl groups lining the intercapsular cavity and the phenyl/naphthyl lateral groups on the intracapsular walls (Figure S19, Supporting Information). These values are consistent with those measured, for example, in the imidazolate framework ZIF-8 and the hydrophobic molecular zeolites.[19a,40h,41] Moreover, the novel materials exhibit a high stability and after several cycles of gas absorption/desorption, the pore volumes of both of the microporous 3D structures are fully preserved.

Solid State NMR Spectroscopy. Solid state NMR spectroscopy is the method of choice to recognize the through-space correlations in the crystalline structures and the interactions of the host matrices with guests.[42] The high resolution ^1H MAS NMR spectra at 600 MHz and fast magic angle spinning (30 kHz) and the 2D $^1H-^{13}C$ HETCOR NMR spectra at different contact times of $[Ag(L^{SNf})]_6(PF_6)_6$ and $[Ag(L^{SPhm\text{-}Me})]_6(PF_6)_6$ were collected to elucidate the porous crystalline architectures and to recognize the CO_2 captured in the cavities. The 2D spectrum collected at short contact times enabled fixing the correlations of the hydrogens directly bonded to carbon nuclei, whereas the spectra with longer contact times showed the interactions at longer distances (within 5 Å).[43] In the 2D NMR spectrum with a contact time as short as 50 μs of the $[Ag(L^{SNf})]_6(PF_6)_6$ (Figure 10a), the correlation of the chemical shifts in the hydrogen and carbon domains allowed us to assign the 1D ^1H and ^{13}C MAS spectra of the compound. A striking observation is that the signal of the methyl group H41 resonates considerably upfield in the hydrogen domain δ_H = −0.9 ppm. This result is a strong indication for a magnetic susceptibility effect of the neighboring aromatic groups facing the methyl C41 at a short distance of approximately 3 Å and the presence of CH···π interactions, which is consistent with the crystal structure.[44] The CH···π arrangement is shown in the molecular structure presented beside Figure 10a. At a longer contact time of 0.5 ms, the 2D spectrum highlighted the further intramolecular interactions, which are consistent with the molecular structure and the conformations of the ligands (Figure 10b). For example, the two cross-peaks marked in red represent the interactions between H51−C21 and H42−C22 within the pyrazole ring, whereas the region marked in blue indicates the cross-peaks from the aromatic hydrogens to the methyl carbons C42 and C51. The cross-peaks marked in orange show the interaction between the pyrazole hydrogen H21 and the Nf carbons. These intramolecular cross-peaks,

dx.doi.org/10.1021/ja507555j | J. Am. Chem. Soc. 2014, 136, 14883−14895

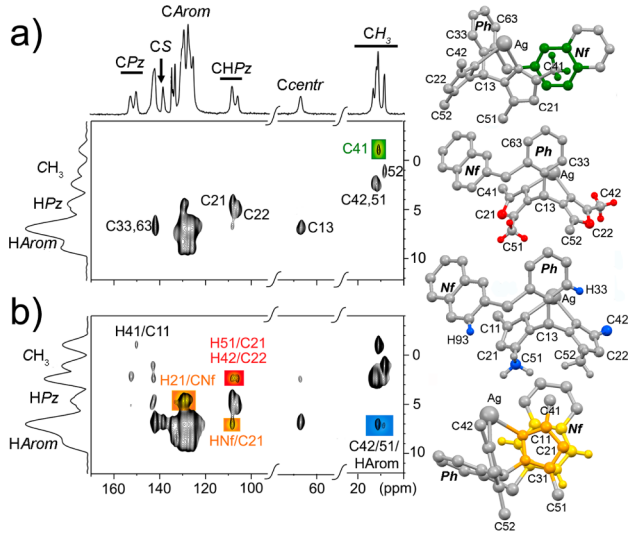

Figure 10. (a) The 2D $^{1}H-^{13}C$ HETCOR NMR spectrum of $Ag(L^{SNf})]_6(PF_6)_6$ at a contact time of 50 μs. The green area highlights the ^{1}H upfield shift due to CH$\cdots\pi$ interaction, as depicted in the molecular structure on the right. (b) The 2D HETCOR spectrum recorded at a contact time of 0.5 ms. The colored areas indicate the through-space hydrogen–carbon close contacts, as highlighted in the molecular structures on the right. The ^{1}H projection and the 1D ^{13}C CP MAS NMR spectrum with a 2 ms contact time are reported.

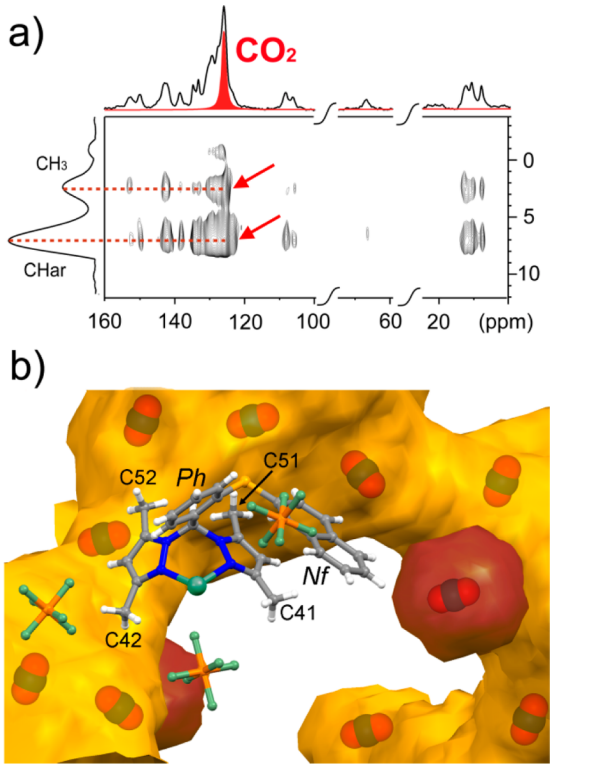

Figure 11. (a) The 2D $^{1}H-^{13}C$ HETCOR NMR spectrum recorded at 250 K and a contact time of 5 ms of $Ag(L^{SNf})]_6(PF_6)_6$ loaded with enriched $^{13}CO_2$. The ^{1}H projection and the 1D ^{13}C CP MAS NMR spectrum with a 5 ms contact time are reported. The through-space correlations of the matrix hydrogens with the CO_2 carbons are indicated. (b) The red and yellow areas represent the surfaces of the intracapsular and intercapsular cavities, respectively, explored by CO_2 (see also Figure 3).

already visible at the contact time of 50 μs, are due to the $\pi-\pi$ stacking between the pyrazole ring and the naphthalene as illustrated beside Figure 10b.

Magic angle spinning NMR could provide the direct demonstration of CO_2 absorbed in the crystalline systems and the accessibility of the cavities in the structure. Once enriched $^{13}CO_2$ is loaded in the porous materials, intense cross-peaks appear between the carbons of CO_2 (which do not possess hydrogens) and the hydrogens of the host, demonstrating the close proximity of the carbon dioxide molecules with the porous matrix walls at a distance of less than 5 Å (Figure 11a). At the low temperature of the 2D NMR experiments (250 K), the nuclear dipolar interaction becomes more efficient and the through-space magnetization transfer under the cross-polarization conditions occurs from the host hydrogens to the CO_2 carbon nuclei because of a sufficiently long residence time of the CO_2 within the cavities.[19a] Therefore, the intense signal of CO_2 in the carbon spectrum, as observed in Figure 11a for $[Ag(L^{SNf})]_6(PF_6)_6$ (highlighted in red), is a clear demonstration of CO_2 capture by the crystalline structure and of the open porosity of the framework.

In the sample $[Ag(L^{SPhm\text{-}Me})]_6(PF_6)_6$ wherein large intracapsular voids are present, we collected a 2D $^{1}H-^{13}C$ NMR spectrum with a contact time as short as 1 ms to detect the specific interactions of CO_2 at shorter distances with the individual ligand moieties (Figure 12a). Notably, CO_2 strongly correlates with the methyl hydrogens of the peripheral group (Phm-Me), which indicates the center of the intracapsular space (as highlighted in red in Figure 12c). This result demonstrates that CO_2 is loaded in the intracapsular cavities, which represent a 0.3 fraction of the pore capacity. At longer contact times (Figure 12b), the magnetization transfer to CO_2 arises from the entire population of hydrogens of the ligand and generates a prominent CO_2 carbon signal, highlighting that the CO_2 molecules pervade the intra- and intercapsular cavities.

CONCLUSIONS

In the present contribution, we investigated the structural aspects of silver-based coordination polymers and metallacycles constructed by bispyrazole ligands, opportunely modified to modulate the structure and porosity of the materials. These factors played a key role in the outcome of the diverse structural features regarding the ligand shape and the chelation properties, the presence of side groups, the metal node coordination and the type of counterions. The ligand and the metal topology generally determine the formation of the cyclic or the polymeric structures (chains), which exhibit the invariant feature of being sustained by the molecular bridges of the ligands. The coordination polymeric chain formation can be idealized as a ring opening of the metallacycle with a consequent conformational twist, which induces polymerization to helicoidal chains. Despite the significant differences between the overall structural arrangements of the hexamers and the chains, the local environment of the AgL fragment is substantially coincident in all of the structures reported in this study (Figure S2, Supporting Information). This result is because of the intrinsic flexibility of the metal geometry that can be adopted by silver(I). However, the presence of the phenyl ring directly attached to the bispyrazole scaffold imparts a structural rigidity and preorganization of the ligand that guarantees an invariant bridging behavior to the metal centers. This behavior occurs even with markedly different functionalization of the peripheral aromatic moieties (Phm-Me, Php-Me

dx.doi.org/10.1021/ja507555j | J. Am. Chem. Soc. 2014, 136, 14883–14895

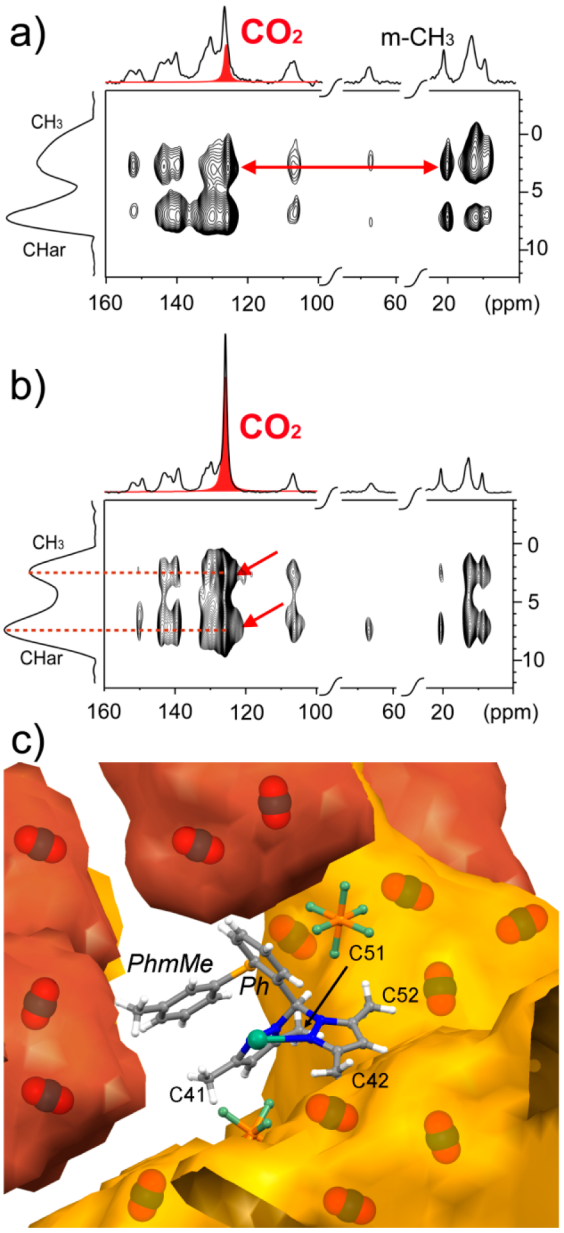

Figure 12. (a) The 2D HETCOR spectrum of $[Ag(L^{SPhm\text{-}Me})]_6(PF_6)_6$ loaded with enriched $^{13}CO_2$ recorded at 250 K and a contact time of 1 ms. The double arrow indicates the correlation of the Phm-Me methyl hydrogens with the CO_2 carbons. (b) The spectrum of the same sample recorded with a contact time of 5 ms. (c) The red and yellow areas represent the surfaces of the intracapsular and intercapsular cavities, respectively, explored by CO_2 (see also Figure 3).

Ph-F, PhOMe, and Nf). Therefore, it can be concluded that the lateral groups can be substituted without changing the main structural architecture. A crucial role is played by the counteranions (PF_6^- and $CF_3SO_3^-$). PF_6^- is highly symmetric but weakly coordinating (a poor Lewis base), whereas $CF_3SO_3^-$ is capable of a stronger interaction with the metal centers, but it has a low symmetry. Despite the weak nature of the Ag···F interaction, the octahedral symmetry of PF_6^- is suitable for the crystallization of the hexameric metallacycles in a highly symmetric cubic space group. A comparison of the cubic crystalline structures reveals that the interactions of PF_6^- with the metal centers (Ag···F) and the ligand fragments (C–H···F) overcome the energetic contributions provided by the peripheral aromatic functionalization. In the hexameric metallacycles, one of the PF_6^- anions bridges two metal cations, whereas the $CF_3SO_3^-$ consistently interacts with a metal ion in a monodentate fashion in all of the coordination polymeric chain structures. The hexameric rings can self-assemble at a further hierarchical level into supramolecular capsules formed by four rings, with the shape of a nanoscale tetrahedron. The opportunity to exploit two hierarchical levels of supramolecular organization results in two types of cavities, an intracapsular cavity and an intercapsular cavity. The latter cavity constitutes the main vessel for storing gases, whereas the intracapsular space can be modulated by the bulkiness of the side residues of the ligand. Thus, this framework is at the origin of an extended network of interconnected porosity, which successfully reversibly captured gases and vapors. In fact, the supramolecular structures based on hexameric molecules exhibited permanent porosity as demonstrated by CO_2 adsorption isotherms and proved to be selective in favor of CO_2 with respect to N_2 and CH_4.

A direct observation of carbon dioxide confined to the cavities could be obtained by MAS NMR. The spatial proximity of the gas to the matrix walls over the range of a few Angstroms was proven by the considerable magnetization transfer from the matrix hydrogen nuclei to the CO_2 carbon nuclei. The 2D HETCOR NMR experiments could detect the gas molecules that reside in close contact with the matrix walls by intense cross-correlation peaks in the hydrogen–carbon map. Moreover, solid-state NMR spectroscopy could identify CO_2 molecules interacting with methyl or phenyl groups in two distinct cavities and recognize that both the intercapsular and the intracapsular spaces can be explored by diffusing CO_2.

■ ASSOCIATED CONTENT

Supporting Information

Synthesis, crystallographic details, CIF files (CCDC 1014232–1014242), Hirshfeld analysis and fingerprint plots, molecular structure of the model complex $[Ag(L^{SPhp\text{-}Me})]_6(PF_6)_6$, variable temperature powder XRD, thermal analyses for $[Ag(L^{SPhm\text{-}Me})]_6(PF_6)_6$ and $Ag(LSNf)]_6(PF_6)_6$, heat of adsorptions and IAST curves, solid state NMR. This material is available free of charge via the Internet at http://pubs.acs.org.

■ AUTHOR INFORMATION

Corresponding Authors

angiolina.comotti@mater.unimib.it
marchio@unipr.it

Notes

The authors declare no competing financial interest.

■ ACKNOWLEDGMENTS

This study was supported by the Università degli Studi di Parma (Parma, Italy). A.C. would like to thank Fondazione Cariplo 2012 and MIUR (PRIN 2011).

■ REFERENCES

(1) (a) Sun, Q. F.; Iwasa, J.; Ogawa, D.; Ishido, Y.; Sato, S.; Ozeki, T.; Sei, Y.; Yamaguchi, K.; Fujita, M. *Science* **2010**, *328*, 1144–1147. (b) Sun, Q. F.; Sato, S.; Fujita, M. *Nat. Chem.* **2012**, *4*, 330–333. (c) Dalgarno, S. J.; Power, N. P.; Atwood, J. L. *Coord. Chem. Rev.* **2008**, *252*, 825–841. (d) Mal, P.; Breiner, B.; Rissanen, K.; Nitschke, J. R. *Science* **2009**, *324*, 1697–1699. (e) Caulder, D. L.; Raymond, K. N. *Acc. Chem. Res.* **1999**, *32*, 975–982.

(2) (a) Khlobystov, A. N.; Blake, A. J.; Champness, N. R.; Lemenovskii, D. A.; Majouga, A. G.; Zyk, N. V.; Schroder, M. *Coord. Chem. Rev.* **2001**, *222*, 155−192. (b) Robin, A. Y.; Fromm, K. M. *Coord. Chem. Rev.* **2006**, *250*, 2127−2157. (c) Janiak, C.; Vieth, J. K. *New J. Chem.* **2010**, *34*, 2366−2388. (d) Leong, W. L.; Vittal, J. J. *Chem. Rev.* **2011**, *111*, 688−764. (e) Liu, Y. Z.; Hu, C. H.; Comotti, A.; Ward, M. D. *Science* **2011**, *333*, 436−440. (f) Yan, X. Z.; Li, S. J.; Pollock, J. B.; Cook, T. R.; Chen, J. Z.; Zhang, Y. Y.; Ji, X. F.; Yu, Y. H.; Huang, F. H.; Stang, P. J. *Proc. Natl. Acad. Sci. U. S. A.* **2013**, *110*, 15585−15590. (h) Cook, T. R.; Zheng, Y. R.; Stang, P. J. *Chem. Rev.* **2013**, *113*, 734−777. (i) Inokuma, Y.; Yoshioka, S.; Fujita, M. *Angew. Chem., Int. Ed.* **2010**, *49*, 8912−8914. (l) Farha, O. K.; Spokoyny, A. M.; Mulfort, K. L.; Galli, S.; Hupp, J. T.; Mirkin, C. A. *Small* **2009**, *5*, 1727−1731. (m) Kitagawa, S.; Matsuda, R. *Coord. Chem. Rev.* **2007**, *251*, 2490−2509. (n) Kitagawa, S.; Kitaura, R.; Noro, S. *Angew. Chem., Int. Ed.* **2004**, *43*, 2334−2375. (o) Li, Z.-Y.; Zhang, Y.; Zhang, C.-W.; Chen, L.-J.; Wang, C.; Tan, H.; Yu, Y.; Li, X.; Yang, H.-B. *J. Am. Chem. Soc.* **2014**, *136*, 8577−8589.

(3) Uemura, T.; Yanai, N.; Kitagawa, S. *Chem. Soc. Rev.* **2009**, *38*, 1228−1236.

(4) (a) Rowsell, J. L. C.; Spencer, E. C.; Eckert, J.; Howard, J. A. K.; Yaghi, O. M. *Science* **2005**, *309*, 1350−1354. (b) Wu, H.; Zhou, W.; Yildirim, T. *J. Am. Chem. Soc.* **2009**, *131*, 4995−5000. (c) Kitagawa, S. *Nature* **2006**, *441*, 584−585.

(5) (a) Seward, C.; Jia, W. L.; Wang, R. Y.; Enright, G. D.; Wang, S. N. *Angew. Chem., Int. Ed.* **2004**, *43*, 2933−2936. (b) Xie, Z. G.; Ma, L. Q.; deKrafft, K. E.; Jin, A.; Lin, W. B. *J. Am. Chem. Soc.* **2010**, *132*, 922−923.

(6) (a) Yuan, M.; Zhao, F.; Zhang, W.; Wang, Z. M.; Gao, S. *Inorg. Chem.* **2007**, *46*, 11235−11242. (b) Li, B.; Gu, W.; Zhang, L. Z.; Qu, J.; Ma, Z. P.; Liu, X.; Liao, D. Z. *Inorg. Chem.* **2006**, *45*, 10425−10427.

(7) Imaz, I.; Rubio-Martinez, M.; Garcia-Fernandez, L.; Garcia, F.; Ruiz-Molina, D.; Hernando, J.; Puntes, V.; Maspoch, D. *Chem. Commun.* **2010**, *46*, 4737−4739.

(8) Northrop, B. H.; Zheng, Y. R.; Chi, K. W.; Stang, P. J. *Acc. Chem. Res.* **2009**, *42*, 1554−1563.

(9) (a) Comba, P.; Schiek, W. *Coord. Chem. Rev.* **2003**, *238*, 21−29. (b) Comba, P.; Kerscher, M.; Lawrance, G. A.; Martin, B.; Wadepohl, H.; Wunderlich, S. *Angew. Chem., Int. Ed.* **2008**, *47*, 4740−4743. (c) Comba, P.; Morgen, M.; Wadepohl, H. *Inorg. Chem.* **2013**, *52*, 6481−6501.

(10) Leininger, S.; Olenyuk, B.; Stang, P. J. *Chem. Rev.* **2000**, *100*, 853−907.

(11) Bassanetti, I.; Mezzadri, F.; Comotti, A.; Sozzani, P.; Gennari, M.; Calestani, G.; Marchio, L. *J. Am. Chem. Soc.* **2012**, *134*, 9142−9145.

(12) (a) Janssen, F. F. B. J.; Veraart, L. P. J.; Smits, J. M. M.; de Gelder, R.; Rowan, A. E. 1. *Cryst. Growth Des.* **2011**, *11*, 4313−4325. (b) Awaleh, M. O.; Badia, A.; Brisse, F. *Cryst. Growth Des.* **2006**, *6*, 2674−2685. (c) Carnes, M. E.; Lindquist, N. R.; Zakharov, L. N.; Johnson, D. W. *Cryst. Growth Des.* **2012**, *12*, 1579−1585. (d) Halper, S. R.; Do, L.; Stork, J. R.; Cohen, S. M. *J. Am. Chem. Soc.* **2006**, *128*, 15255−15268. (e) Janiak, C.; Uehlin, L.; Wu, H. P.; Klüfers, P.; Piotrowski, H.; Scharmann, T. G. *J. Chem. Soc., Dalton Trans.* **1999**, 3121−3131. (f) Wu, H. P.; Janiak, C.; Rheinwald, G.; Lang, H. *J. Chem. Soc., Dalton Trans.* **1999**, 183−190. (g) Caballero, A. B.; Maclaren, J. K.; Rodriguez-Dieguez, A.; Vidal, I.; Dobado, J. A.; Salas, J. M.; Janiak, C. *Dalton Trans.* **2011**, *40*, 11845−11855.

(13) (a) Sekiya, R.; Fukuda, M.; Kuroda, R. *J. Am. Chem. Soc.* **2012**, *134*, 10987−10997. (b) Mukherjee, G.; Biradha, K. *Cryst. Growth Des.* **2013**, *13*, 4100−4109.

(14) (a) Chakraborty, B.; Halder, P.; Paine, T. K. *Dalton Trans.* **2011**, *40*, 3647−3654. (b) Little, M. A.; Halcrow, M. A.; Harding, L. P.; Hardie, M. J. *Inorg. Chem.* **2010**, *49*, 9486−9496. (c) Libri, S.; Mahler, M.; Espallargas, G. M.; Singh, D. C. N. G.; Soleimannejad, J.; Adams, H.; Burgard, M. D.; Rath, N. P.; Brunelli, M.; Brammer, L. *Angew. Chem., Int. Ed.* **2008**, *47*, 1693−1697. (d) Steel, P. J.; Fitchett, C. M. *Coord. Chem. Rev.* **2008**, *252*, 990−1006. (e) Uemura, K.; Kumamoto, Y.; Kitagawa, S. *Chem.—Eur. J.* **2008**, *14*, 9565−9576. (f) Niu, C. Y.; Wu, B. L.; Zheng, X. F.; Zhang, H. Y.; Li, Z. J.; Hou, H. W. *Dalton Trans.* **2007**, 5710−5713. (g) Zhang, J. P.; Horike, S.; Kitagawa, S. *Angew. Chem., Int. Ed.* **2007**, *46*, 889−892. (h) Jouaiti, A.; Hosseini, M. W.; Kyritsakas, N.; Grosshans, P.; Planeix, J. M. *Chem. Commun.* **2006**, 3078−3080. (i) Nagarathinam, M.; Vittal, J. J. *Angew. Chem., Int. Ed.* **2006**, *45*, 4337−4341.

(15) (a) Esteban, J.; Font-Bardia; Escuer, A. *Inorg. Chem.* **2014**, *53*, 1113−1121. (b) Iengo, E.; Zangrando, E.; Alessio, E. *Acc. Chem. Res.* **2006**, *39*, 841−851. (c) Mezei, G.; Baran, P.; Raptis, R. G. *Angew. Chem., Int. Ed.* **2004**, *43*, 574−577. (d) Li, G.; Yu, W. B.; Ni, J.; Liu, T. F.; Liu, Y.; Sheng, E. H.; Cui, Y. *Angew. Chem., Int. Ed.* **2008**, *47*, 1245−1249. (e) Wang, G. L.; Lin, Y. J.; Berke, H.; Jin, G. X. *Inorg. Chem.* **2010**, *49*, 2193−2201. (f) Vajpayee, V.; Song, Y. H.; Cook, T. R.; Kim, H.; Lee, Y.; Stang, P. J.; Chi, K. W. *J. Am. Chem. Soc.* **2011**, *133*, 19646−19649. (g) Chakrabarty, R.; Mukherjee, P. S.; Stang, P. J. *Chem. Rev.* **2011**, *111*, 6810−6918. (h) Xu, J.; Raymond, K. N. *Angew. Chem., Int. Ed.* **2000**, *39*, 2745−2747. (i) Gao, C. Y.; Zhao, L.; Wang, M. X. *J. Am. Chem. Soc.* **2011**, *133*, 8448−8451. (l) Zhu, B. X.; Zhang, Q. L.; Zhang, Y. Q.; Zhu, T.; Clegg, J. K.; Lindoy, L. F.; Wei, G. *Inorg. Chem.* **2008**, *47*, 10053−10061.

(16) (a) Pietrass, T.; Cruz-Campa, I.; Kombarakkaran, J.; Sirimulla, S.; Arif, A. M.; Noveron, J. C. *J. Phys. Chem. C* **2010**, *114*, 21371−21377. (b) Chatterjee, B.; Noveron, J. C.; Resendiz, M. J. E.; Liu, J.; Yamamoto, T.; Parker, D.; Cinke, M.; Nguyen, C. V.; Arif, A. M.; Stang, P. J. *J. Am. Chem. Soc.* **2004**, *126*, 10645−10656. (c) Li, G.; Yu, W. B.; Cui, Y. *J. Am. Chem. Soc.* **2008**, *130*, 4582−4583.

(17) (a) Mondal, S. S.; Bhunia, A.; Kelling, A.; Schilde, U.; Janiak, C.; Holdt, H. J. *Chem. Commun.* **2014**, *50*, 5441−5443. (b) Mondal, S. S.; Bhunia, A.; Kelling, A.; Schilde, U.; Janiak, C.; Holdt, H. J. *J. Am. Chem. Soc.* **2014**, *136*, 44−47.

(18) (a) Bassanetti, I.; Marchio, L. *Inorg. Chem.* **2011**, *50*, 10786−10797. (b) Gennari, M.; Bassanetti, I.; Marchio, L. *Polyhedron* **2010**, *29*, 361−371.

(19) (a) Comotti, A.; Fraccarollo, A.; Bracco, S.; Beretta, M.; Distefano, G.; Cossi, M.; Marchese, L.; Riccardi, C.; Sozzani, P. *CrystEngComm* **2013**, *15*, 1503−1507. (b) Bracco, S.; Comotti, A.; Valsesia, P.; Chmelka, B. F.; Sozzani, P. *Chem. Commun.* **2008**, 4798−4800. (c) Sozzani, P.; Bracco, S.; Comotti, A.; Ferretti, L.; Simonutti, R. *Angew. Chem., Int. Ed.* **2005**, *44*, 1816−1820.

(20) Peterson, L. K.; Kiehlmann, E.; Sanger, A. R.; The, K. I. *Can. J. Chem.* **1974**, *52*, 2367−2374.

(21) Heynderickx, A.; Samat, A.; Guglielmetti, R. *J. Heterocycl. Chem.* **2001**, *38*, 737−742.

(22) *SMART (Control) and SAINT (Integration) Software for CCD Systems*; Bruker AXS: Madison, WI, 1994.

(23) *Area-Detector Absorption Correction*; Siemens Industrial Automation, Inc.: Madison, WI, 1996.

(24) Altomare, A.; Burla, M. C.; Camalli, M.; Cascarano, G. L.; Giacovazzo, C.; Guagliardi, A.; Moliterni, A. G. G.; Polidori, G.; Spagna, R. *J. Appl. Crystallogr.* **1999**, *32*, 115−119.

(25) Burla, M. C.; Caliandro, R.; Camalli, M.; Carrozzini, B.; Cascarano, G. L.; De Caro, L.; Giacovazzo, C.; Polidori, G.; Spagna, R. *J. Appl. Crystallogr.* **2005**, *38*, 381−388.

(26) Sheldrick, G. M. *SHELX97: Programs for Crystal Structure Analysis*, Release 97−2; University of Göttingen: Göttingen, Germany, 1997.

(27) Farrugia, L. J. *J. Appl. Crystallogr.* **1999**, *32*, 837−838.

(28) Spek, A. L. *Acta Crystallogr., Sect. D: Biol. Crystallogr.* **2009**, *D65*, 148−155.

(29) Macrae, C. F.; Edgington, P. R.; McCabe, P.; Pidcock, E.; Shields, G. P.; Taylor, R.; Towler, M.; van de Streek, J. *J. Appl. Crystallogr.* **2006**, *39*, 453−457.

(30) (a) Spackman, M. A.; Jayatilaka, D. *CrystEngComm* **2009**, *11*, 19−32. (b) McKinnon, J. J.; Jayatilaka, D.; Spackman, M. A. *Chem. Commun.* **2007**, 3814−3816.

(31) Wolff, S. K.; Grimwood, D. J.; McKinnon, J. J.; Turner, M. J.; Jayatilaka, D.; Spackman, M. A. *CrystalExplorer*, Version 3.1; University of Western Australia: Perth, 2012.

(32) As indexes of structural rigidity/flexibility of these ligands it is convenient to compare the values of the torsion angle τ and the dihedral planes α and β, see Figure S1 (Supporting Information). The τ angle varies in the narrow range of 0.8−1.4° (hexamers) and 0.6−6.7° (chains), whereas the β angle varies in the narrow range 10.8−15.4° for the hexameric complexes, and in the wider range 9.7−42.3° for the coordination polymeric chains.
(33) The volume of the unit cell cavities were calculated by rolling a sphere of 3.2 Å diameter on the molecular surface, by using the Mercury 3.1 program.
(34) Fromm, K. M.; Doimeadios, J. L. S.; Robin, A. Y. *Chem. Commun.* **2005**, 4548−4550.
(35) (a) Moulton, B.; Zaworotko, M. J. *Chem. Rev.* **2001**, *101*, 1629−1658. (b) Zhang, J. P.; Huang, X. C.; Chen, X. M. *Chem. Soc. Rev.* **2009**, *38*, 2385−2396. (c) Brog, J. P.; Chanez, C. L.; Crochet, A.; Fromm, K. M. *RSC Adv.* **2013**, *3*, 16905−16931.
(36) Carlucci, L.; Ciani, G.; Garcia-Ruiz, J. M.; Moret, M.; Proserpio, D. M.; Rizzato, S. *Cryst. Growth Des.* **2009**, *9*, 5024−5034.
(37) Wang, Y.; He, C. T.; Liu, Y. J.; Zhao, T. Q.; Lu, X. M.; Zhang, W. X.; Zhang, J. P.; Chen, X. M. *Inorg. Chem.* **2012**, *51*, 4772−4778.
(38) Mayers, A. L.; Prausnitz, J. M. *AIChE J.* **1965**, *11*, 121−127.
(39) (a) Sumida, K.; Rogow, D. L.; Mason, J. A.; McDonald, T. M.; Bloch, E. D.; Herm, Z. R.; Bae, T. H.; Long, J. R. *Chem. Rev.* **2012**, *112*, 724−781. (b) Li, B.; Wang, H.; Chen, B. *Chem.—Asian J.* **2014**, *9*, 1474−1498. (c) Nugent, P.; Belmabkhout, Y.; Burd, S. D.; Cairns, A. J.; Luebke, R.; Forrest, K.; Pham, T.; Ma, S.; Space, B.; Wojtas, L.; Eddaoudi, M.; Zaworotko, M. J. *Nature* **2013**, *495*, 80−84. (d) Liu, J.; Thallapally, P. K.; McGrail, B. P.; Brown, D. R.; Liu, J. *Chem. Soc. Rev.* **2012**, *41*, 2308−2322. (e) Liu, B.; Smit, B. *Langmuir* **2009**, *25*, 5918−5926. (f) Goj, A.; Sholl, D. S.; Akten, E. D.; Kohen, D. *J. Phys. Chem. B* **2002**, *106*, 8367−8375.
(40) (a) Tian, J.; Thallapally, P. K.; McGrail, B. P. *Cryst. Eng. Commun.* **2012**, *14*, 1909−1919. (b) Holst, J. R.; Trewin, A.; Cooper, A. I. *Nat. Chem.* **2010**, *2*, 915−920. (c) Nugent, P. S.; Rhodus, V. L.; Pham, T.; Forrest, K.; Wojtas, L.; Space, B.; Zaworotko, M. J. *J. Am. Chem. Soc.* **2013**, *135*, 10950. (d) Ananchenko, G. S.; Moudrakovski, I. L.; Coleman, A. W.; Ripmeester, J. A. *Angew. Chem., Int. Ed.* **2008**, *47*, 5616−5618. (e) Lim, S.; Kim, H.; Selvapalam, N.; Kim, K.-J.; Cho, S. J.; Seo, G.; Kim, K. *Angew. Chem., Int. Ed.* **2008**, *47*, 3352−3355. (f) Jiang, S.; Bacsa, J.; Wu, X.; Jones, J. T. A.; Dawson, R.; Trewin, A.; Adams, D. J.; Cooper, A. I. *Chem. Commun.* **2011**, *47*, 8919−8921. (g) Tsue, H.; Ishibashi, K.; Tokita, S.; Takahashi, H.; Matsui, K.; Tamura, R. *Chem.—Eur. J.* **2008**, *14*, 6125−6134. (h) Comotti, A.; Bracco, S.; Distefano, G.; Sozzani, P. *Chem. Commun.* **2009**, 284−286. (i) Comotti, A.; Bracco, S.; Yamamoto, A.; Beretta, M.; Hirukawa, T.; Tohnai, N.; Miyata, M.; Sozzani, P. *J. Am. Chem. Soc.* **2014**, *136*, 618−621. (l) Maspero, A.; Giovenzana, G. B.; Masciocchi, N.; Palmisano, G.; Comotti, A.; Sozzani, P.; Bassanetti, I.; Nardo, L. *Cryst. Growth Des.* **2013**, *13*, 4948−4956.
(41) Huang, H. L.; Zhang, W. J.; Liu, D. H.; Liu, B.; Chen, G. J.; Zhong, C. L. *Chem. Eng. Sci.* **2011**, *66*, 6297−6305.
(42) (a) Comotti, A.; Gallazzi, M. C.; Simonutti, R.; Sozzani, P. *Chem. Mater.* **1998**, *10*, 3589−3596. (b) Comotti, A.; Bracco, S.; Sozzani, P.; Horike, S.; Matsuda, R.; Chen, J.; Takata, M.; Kubota, Y.; Kitagawa, S. *J. Am. Chem. Soc.* **2008**, *130*, 13664−13672. (c) Bracco, S.; Comotti, A.; Simonutti, R.; Camurati, I.; Sozzani, P. *Macromolec.* **2002**, *35*, 1677−1684. (d) Bovey, F. A.; Mirau, P. *NMR of Polymers*; Academic Press: San Diego, CA, 1996.
(43) (a) Vinogradov, E.; Madhu, P. K.; Vega, S. *Chem. Phys. Lett.* **1999**, *314*, 443−450. (b) Leskes, M.; Madhu, P. K.; Vega, S. *Chem. Phys. Lett.* **2007**, *447*, 370−374. (c) van Rossum, B. J.; de Groot, C. P.; Ladizhansky, V.; Vega, S.; de Groot, H. J. M. *J. Am. Chem. Soc.* **2000**, *122*, 3465−3472. (d) Sozzani, P.; Bracco, S.; Comotti, A.; Simonutti, R.; Camurati, I. *J. Am. Chem. Soc.* **2003**, *125*, 12881−12893. (e) Comotti, A.; Bracco, S.; Mauri, M.; Mottadelli, S.; Ben, T.; Qiu, S. L.; Sozzani, P. *Angew. Chem., Int. Ed.* **2012**, *51*, 10136−10140. (f) Comotti, A.; Bracco, S.; Valsesia, P.; Ferretti, L.; Sozzani, P. *J. Am. Chem. Soc.* **2007**, *129*, 8566−8576. (g) Brustolon, M.; Barbon, A.; Bortolus, M.; Maniero, A. L.; Sozzani, P.; Comotti, A.; Simonutti, R. *J. Am. Chem. Soc.* **2004**, *126*, 15512−15519. (h) Uemura, T.; Horike, S.; Kitagawa, K.; Mizuno, M.; Endo, K.; Bracco, S.; Comotti, A.; Sozzani, P.; Nagaoka, M.; Kitagawa, S. *J. Am. Chem. Soc.* **2008**, *130*, 6781−6788.
(44) (a) Takahashi, O.; Kohno, Y.; Nishio, M. *Chem. Rev.* **2010**, *110*, 6049−6076. (b) Rapp, A.; Schnell, I.; Sebastiani, D.; Brown, S. P.; Percec, V.; Spiess, H. W. *J. Am. Chem. Soc.* **2003**, *125*, 13284−13297. (c) Sozzani, P.; Comotti, A.; Bracco, S.; Simonutti, R. *Chem. Commun.* **2004**, 768−769. (d) Kobr, L.; Zhao, K.; Shen, Y. Q.; Comotti, A.; Bracco, S.; Shoemaker, R. K.; Sozzani, P.; Clark, N. A.; Price, J. C.; Rogers, C. T.; Michl, J. *J. Am. Chem. Soc.* **2012**, *134*, 10122−10131. (e) Bracco, S.; Comotti, A.; Ferretti, L.; Sozzani, P. *J. Am. Chem. Soc.* **2011**, *133*, 8982−8994. (f) Bracco, S.; Comotti, A.; Valsesia, P.; Beretta, M.; Sozzani, P. *CrystEngComm* **2010**, *12*, 2318−2321. (g) Comotti, A.; Bracco, S.; Sozzani, P.; Hawxwell, S. M.; Hu, C. H.; Ward, M. D. *Cryst. Growth Des.* **2009**, *9*, 2999−3002. (h) Sozzani, P.; Comotti, A.; Bracco, S.; Simonutti, R. *Angew. Chem., Int. Ed.* **2004**, *43*, 2792−2797. (i) Simonutti, R.; Comotti, A.; Negroni, F.; Sozzani, P. *Chem. Mater.* **1999**, *11*, 822−828. (l) Waugh, S.; Fessenden, R. W. *J. Am. Chem. Soc.* **1957**, *79*, 846−849. (m) Johnson, C. E.; Bovey, F. A. *J. Chem. Phys.* **1958**, *29*, 1012−1014. (n) Canceill, J.; Lacombe, L.; Collet, A. *J. Am. Chem. Soc.* **1986**, *108*, 4230−4232.